Accepted manuscript

Biomechanics and Modeling in Mechanobiology

The effective elastic properties of human trabecular bone may be approximated using micro finite element analyses of embedded volume elements

Karol Daszkiewicz [1,2], Ghislain Maquer [1] and Philippe K. Zysset [1]

1. Institute for Surgical Technology and Biomechanics, University of Bern, Switzerland

2. Faculty of Civil and Environmental Engineering, Gdańsk University of Technology, Poland

Corresponding author: Ghislain Maquer (ghislain.maquer@istb.unibe.ch)

Abbreviated title: Effective elastic properties of trabecular bone

Abstract word count: 249

Total word count: 3393

Attachments: 5 figures and 2 tables + 1 figure and 4 tables in the appendices

Disclosure page

The authors have no conflict of interest to report.

Acknowledgments

The script manager Medtool (www.dr-pahr.at) was used to generate the µFE models, start the computations and analyse the results. The authors would like to thank Prof. Bert van Rietbergen for sharing the µCT data. Karol Daszkiewicz is supported by grants from the Faculty of Civil and Environmental Engineering, Gdańsk University of Technology. The Swiss National Foundation (grant n° 143769) and the Gebert Rüf Foundation (GRS-079/14) are also gratefully acknowledged.

Abstract

Boundary conditions (BCs) and sample size affect the measured elastic properties of cancellous bone. Samples too small to be representative appear stiffer under kinematic uniform BCs (KUBCs) than under periodicity-compatible mixed uniform BCs (PMUBCs). To avoid those effects, we propose to determine the effective properties of trabecular bone using an embedded configuration. Cubic samples of various sizes (2.63, 5.29, 7.96, 10.58 and 15.87 mm) were cropped from µCT scans of femoral heads and vertebral bodies. They were converted into µFE models and their stiffness tensor was established via six uniaxial and shear load cases. PMUBCs- and KUBCs- based tensors were determined for each sample. "*In situ"* stiffness tensors were also evaluated for the embedded configuration, i.e. when the loads were transmitted to the samples via a layer of trabecular bone. The Zysset-Curnier model accounting for bone volume fraction and fabric anisotropy was fitted to those stiffness tensors and model parameters ν_0 (Poisson's ratio), E_0 and μ_0 (elastic and shear moduli) were compared between sizes. BCs and sample size had little impact on ν_0. However, KUBCs- and PMUBCs-based E_0 and μ_0 respectively decreased and increased with growing size, though convergence was not reached even for our largest samples. Both BCs produced upper and lower bounds for the *in situ* values that were almost constant across samples dimensions, thus appearing as an approximation of the effective properties. PMUBCs seem also appropriate for mimicking the trabecular core, but they still underestimate its elastic properties (especially in shear) even for nearly orthotropic samples.

Keywords: trabecular bone, elastic properties, boundary conditions, micro finite elements, in situ, embedded configuration

1. Introduction

Osteoporosis is a widespread skeleton disease responsible for deleterious fractures in the elderly population (e.g. Hadji et al. 2013). Substantial direct and indirect social and economic costs are associated with those fractures, which emphasize the need for prevention and treatment of the osteoporotic disease. In this context, *in silico* medicine may prove an asset (Viceconti 2015). After all, homogenized FE (hFE) models can be used for diverse clinical applications such as the prediction of bone strength (Zysset et al. 2013), the evaluation of drug therapies (Keaveny et al. 2014), the optimisation of osteosynthesis procedures (Synek et al. 2015) or the prediction of the mechanical impact of osteoplasty (Maquer et al. 2016). In contrast to micro finite element (μFE) analysis based on microcomputed tomography (μCT) images, hFE analysis - the current option to exploit clinical CT images - relies on averaged material properties of trabecular bone elements.

The elastic properties of representative volume elements (RVE) of trabecular bone may in turn be computed from μFE analyses using a homogenization procedure (Hollister et al. 1991). The technique requires μCT data and sufficient computational resources, but allows multiple loading scenarios per sample without being affected by experimental damage-artefacts. Homogenization theory is more accurate for periodic porous composites than standard approaches (Hollister and Kikuchi 1992). For non-periodic composites as trabecular bone, the Hill condition, equivalence between strain energy at macro- and micro- levels (Hill 1963), is only fulfilled for kinematic uniform (KUBCs: uniform displacements at the boundaries), static uniform (SUBCs: uniform tractions) and mixed uniform boundary conditions (MUBCs: combination of uniform tractions and displacements) (Hazanov and Amieur 1995, Ostoja-Starzewski 2006). More recently, Pahr and Zysset (2008) also proposed the periodicity-compatible MUBCs (PMUBCs) to mimic periodic BCs on nearly orthotropic structures.

The dimension of human bones often prevents the creation of RVEs and only apparent properties can be calculated for volumes of a non-periodic material that are too small to be representative (Hazanov and Huet 1994). Unlike the effective properties, the apparent ones are affected by the boundary conditions. Yet, a multitude of embedding approaches can smoothen this impact and relax the periodicity constraints (Böhm 2016). The idea is to measure the properties of a core region embedded in larger outer region on which loads are applied. The outer region acts as a buffer transferring the loads to the core in a more "natural" way. Although such analyses are commonly done for composites, we are not aware of its application to bone.

A size-dependent behaviour was also noted experimentally for foams (Lakes 1983, Hütter 2016), concrete (Syroka-Korol et al. 2013) and biological tissues (Choi et al. 1990) and also numerically for random matrix-inclusion composites (Ostoja-Starzewski 1998), periodic composites (Pecullan et al. 1999, Wang et al. 2009) and unidirectional fibre reinforced composites (Jiang et al. 2001). This behaviour may be described by the micropolar (or Cosserat) elasticity (Eringen 1999) as a dependence on the ratio of the dimension of the volume element to the characteristic length of its inner micro-structure (Wheel et al. 2015). Yet, it remains difficult to dissociate the influence of BCs and size on the apparent properties.

Using a randomly generated structure mimicking cancellous bone, Blöß and Welsch (2015) showed that KUBCs and SUBCs provided upper and lower bounds to PMUBCs-based elastic modulus. These bounds slowly converged towards the PMUBCs value with increasing sample size. In this work, the PMUBCs-based modulus was relatively unaffected by the sample size and was considered as a possible approximation of the effective modulus. However, this result might not hold for real bone morphologies.

We propose to use an embedding approach to determine the elastic properties of a trabecular region when loads are transmitted to the volume of interest via an outer layer of bone (Fig.

1a). Our hypothesis is that these apparent elastic properties actually converge towards "*in situ*" values if the outer layer gets sufficiently large (Fig. 1b). Then, using samples of different dimensions, the present study aims to establish the size-dependency of the *in situ*, KUBCs and PMUBCs-based elastic properties.

2. Materials and methods

2.1. Preparation of the samples

Microcomputed tomography (μCT) images (37μm voxel size) performed on femoral heads and vertebral bodies were obtained from two previous studies (Lochmüller et al. 2008, Marangalou et al. 2013). The donors had dedicated their body by testament to the Institute of Anatomy of the LMU in Munich or the Institute of Anatomy of the Amsterdam Medical Center (AMC) during life after ethics approval for the purpose of teaching and research. Seven trabecular biopsies were extracted from the vertebral scans (4 male and 2 female donors, 70 ± 6.5 yrs) and thirteen from the femoral ones (2 female donors, 81 and 95 years). Those twenty trabecular regions were segmented using a single-level threshold (Riedler and Calvard 1978) and the mean intercept length (MIL) (Whitehouse 1974, Harrigan and Mann 1984) was used to determine their fabric tensor. The images were then rotated to align the eigenvectors of the fabric tensor with the loading directions, as needed for PMUBCs (Pahr and Zysset 2008). After rotation, 20 cubic volumes of each size (2.63, 5.29, 7.96, 10.58 and 15.87 mm side length) were cropped and cleaned from unconnected bone regions (Fig. 2). BV/TV and degree of anisotropy (DA as ratio of the largest and the smallest eigenvalues of the fabric tensor) of each cube were finally evaluated. Because of morphological dissimilarities between samples extracted from vertebrae and femurs, two data sets were defined: the femur data set composed of 65 cubes (13 scans × 5 sizes) and the complete data set including 100 cubes from both vertebral and femoral sites. Please note that since some of our cubes are too small to be called RVEs, we rather used the term "CVE" for cubic volume

element.

2.2. Computation of the KUBCs- and PMUBCs-based stiffness tensors

The first step was to conduct µFE analyses on the different sizes of CVE using KUBCs and PMUBCs (Fig. 2). To do so, we generated µFE models by converting bone voxels into linear hexahedral elements with isotropic elastic properties (elastic modulus E=10 GPa, Poisson's ratio ν=0.3) (Pistoia et al. 2002). Marrow elements were not included in the µFE models to reduce the computing time and avoid convergence issues due to a high contrast of their stiffness to the stiffness of bone. Linear µFE analyses were performed via the ParOSol solver (Flaig 2012) with three uniaxial and three shear load cases conducted under KUBCs and PMUBCs as described in a previous study (Pahr and Zysset 2008), leading to 1200 simulations. The full stiffness tensors $\mathbf{S}^{\mathrm{KUBCs}}$ and $\mathbf{S}^{\mathrm{PMUBCs}}$ were derived from the µFE analyses via the apparent stresses and strains (Pahr and Zysset 2008) for each CVE.

2.3. Computation of the stiffness tensor of the CVEs in embedded configuration

The second step was to compute the stiffness tensors of the CVEs embedded in a larger volume. For that, we actually used µFE analyses performed on larger CVEs and simply focused on a region of the inner core (Fig. 2). This also means that the loading in embedded configuration was not performed for our largest CVEs (15.87 mm).

Marrow was not included in the µFE analyses, although in principle, its deformation is necessary for the apparent strain calculation. This is a minor issue when BCs are applied directly on the boundary of the CVE as the a priori strains defined by the load case can be used in that case. However, we have no prior knowledge of the deformations occurring at the boundary of an embedded CVE (Fig. 1). Hence, we propose to estimate the deformation of a virtual marrow phase from those of the bone phase. The mean strains for a given CVE of side length L were determined as:

$$\left\langle \varepsilon_{ij} \right\rangle = \frac{1}{V}\int_{\Omega}\frac{1}{2}\left(u_{i,j}+u_{j,i}\right)\mathrm{d}\Omega = \frac{1}{2V}\int_{\Gamma^*}\left(u_i n_j + u_j n_i\right)\mathrm{d}\Gamma^* \tag{1}$$

where Γ^* is the boundary of the embedded CVE. The displacements (u) of a specified face (east, west, bottom, top, south and north, see Fig. 3a) were calculated as the mean displacements of the equally distributed existing bone nodes and virtual marrow points. The displacements for the marrow points $\bar{u}$ were interpolated based on the values from the closest bone nodes in each direction (Fig. 3b).

$$\bar{u} = \frac{1}{\sum N_i}\sum_{i=1}^{6} N_i u^i,\ N_i = \frac{1}{l_i} \tag{1}$$

In the eventuality of a missing bone node in a given direction, the a priori displacements of the point located on the outer face were used in the interpolation. If the a priori displacement component was not specified on the outer face either, the value in the opposite direction was then neglected.

For example, the average shear strain $\langle \varepsilon_{12} \rangle$ was derived as follow:

$$\begin{aligned}\left\langle \varepsilon_{12} \right\rangle &= \frac{1}{2V}\left[\int_{\mathrm{E+W}}\left({}^{\mathrm{E}}u_2 - {}^{\mathrm{W}}u_2\right)\mathrm{d}A + \int_{\mathrm{N+S}}\left({}^{\mathrm{N}}u_1 - {}^{\mathrm{S}}u_1\right)\mathrm{d}A\right] = \\ &= \frac{1}{2V}\left[\sum_{k=1}^{N}\left({}^{\mathrm{E}}u_2^k - {}^{\mathrm{W}}u_2^k\right)\Delta A + \sum_{k=1}^{N}\left({}^{\mathrm{N}}u_1^k - {}^{\mathrm{S}}u_1^k\right)\Delta A\right]\end{aligned} \tag{3}$$

where $\int_{\mathrm{N+S}} \ldots$ is the integral of the displacements of the N square areas ΔA on the north and south face of the CVE. The displacements u^k of the k^{th} square area were calculated as average from corner values of bone nodes and virtual marrow points. Finally, $\langle \varepsilon_{12} \rangle$ were computed based on the average displacements of the face $\langle u_k \rangle$:

$$\begin{aligned}\left\langle \varepsilon_{12} \right\rangle &= \frac{1}{2V}\left[\sum_{k=1}^{N}\left(\frac{{}^{\mathrm{E}}u_2^k}{N} - \frac{{}^{\mathrm{W}}u_2^k}{N}\right)N\Delta A + \sum_{k=1}^{N}\left(\frac{{}^{\mathrm{N}}u_1^k}{N} - \frac{{}^{\mathrm{S}}u_1^k}{N}\right)N\Delta A\right] = \\ &= \frac{1}{2L}\left[\sum_{k=1}^{N}\left(\frac{{}^{\mathrm{E}}u_2^k}{N} - \frac{{}^{\mathrm{W}}u_2^k}{N}\right) + \sum_{k=1}^{N}\left(\frac{{}^{\mathrm{N}}u_1^k}{N} - \frac{{}^{\mathrm{S}}u_1^k}{N}\right)\right] = \frac{1}{2L}\left(\left\langle {}^{\mathrm{E}}u_2 \right\rangle - \left\langle {}^{\mathrm{W}}u_2 \right\rangle + \left\langle {}^{\mathrm{N}}u_1 \right\rangle - \left\langle {}^{\mathrm{S}}u_1 \right\rangle\right)\end{aligned} \tag{4}$$

We conducted a verification analysis for twenty 3.44 mm CVEs embedded in 5.29 mm regions. For those, the marrow was explicitly modelled (E_{marrow}=1 MPa, ν_{marrow}=0.3). The strain components resulting from volume average (two-material approach) and the virtual marrow method introduced in this section (only bone nodes were taken into account) were compared.

A stiffness tensor was computed for each embedded CVE using this new strain information and the elements' stresses resulting from the µFE analyses. However, those stiffness tensors still depend on the BCs applied on the outer boundaries ($\mathbf{S}_{\text{embed}}^{\text{KUBCs}}$ and $\mathbf{S}_{\text{embed}}^{\text{PMUBCs}}$). To understand and cancel this influence, we evaluated $\mathbf{S}_{\text{embed}}^{\text{KUBCs}}$ and $\mathbf{S}_{\text{embed}}^{\text{PMUBCs}}$ for various thicknesses of the outer region.

2.4. Computation of the in situ stiffness tensor

The third step was thus to relate each of the 9 independent components of $\mathbf{S}_{\text{embed}}^{\text{KUBCs}}$ and $\mathbf{S}_{\text{embed}}^{\text{PMUBCs}}$ to the thickness of the outer bony layer via two power laws (one for $\mathbf{S}_{\text{embed}}^{\text{KUBCs}}$, another for $\mathbf{S}_{\text{embed}}^{\text{PMUBCs}}$). These two laws were forced to converge towards a common value for a 30 mm-thick layer, which was assumed sufficient to suppress the impact of the outer BCs. This common value constituted the corresponding component of the *in situ* stiffness tensor ($\mathbf{S}^{\text{in situ}}$) that was then rotated according to the coordinate system of the fabric tensor (Gross et al. 2013).

2.5. Fitting of the Zysset-Curnier model to the stiffness tensors

At this point, it should be clear that $\mathbf{S}^{\text{KUBCs}}$, $\mathbf{S}^{\text{PMUBCs}}$ and $\mathbf{S}^{\text{in situ}}$ were computed for all the CVEs smaller than 15.87 mm (Fig. 2). In a last effort, we thus compared the dependency of those stiffness tensors on the CVE size.

A number of theoretical models were proposed to predict the elastic behaviour of trabecular bone from its morphology (Zysset 2003). Among them, the Zysset-Curnier model (Zysset and

Curnier 1995) relates efficiently the stiffness tensor of a CVE to its best determinants: bone volume fraction (BV/TV) literally the amount of bone and fabric anisotropy reflecting its overall orientation distribution (Maquer et al. 2015). The parameters of the Zysset-Curnier model λ_0, λ_0', μ_0 (shear modulus), k, l were fitted to the orthotropic representation of each stiffness tensor ($\mathbf{S}^{\mathrm{KUBCs}}$, $\mathbf{S}^{\mathrm{PMUBCs}}$, $\mathbf{S}^{\mathrm{in\ situ}}$) via a multi-linear regression after log transformation (Gross et al. 2013, Panyasantisuk et al. 2015). The exponents k and l control the influence of BV/TV and fabric anisotropy, respectively. The values of E_0 (elastic modulus) and v_0 (Poisson's ratio) may be calculated based on λ_0, λ_0', μ_0. In the process, k and l were first determined simultaneously for all CVE sizes (2.63, 5.29, 7.96, 10.58 mm side length) and stiffness tensors ($\mathbf{S}^{\mathrm{KUBCs}}$, $\mathbf{S}^{\mathrm{PMUBCs}}$, $\mathbf{S}^{\mathrm{in\ situ}}$) and then fixed to allow the direct comparison of λ_0, λ_0', μ_0, E_0 and v_0 across sizes and tensors. The confidence intervals of the parameters were also calculated.

For further use of the model, parameter sets were also determined individually for each size and stiffness tensor (Appendix A). Comparisons with the literature were also presented in Appendix B. Convergence analyses were finally conducted after reducing the original finite element size from 37 to 18.5 μm to evaluate its impact on the fitted parameters and the Hill condition (Appendix C).

3. Results

3.1. Morphological information

A broad range of BV/TV [0.043-0.406] and DA [1.14-2.07] was obtained. The complete data set (BV/TV=0.194±0.089) was less dense than the femur data set (BV/TV=0.242±0.060), because it contains vertebral samples with low BV/TV. The complete group was slightly more isotropic (DA=1.59±0.018) compared to the femur data set (DA=1.60±0.017). For comparison, our largest study on the topic included samples from femur, radius and vertebra locations and featured a BV/TV of 0.15±0.084 and a DA of 1.57±0.28 (Gross et al. 2013). As

shown in Table 1, BV/TV and DA were consistent across VE sizes. The lowest values of morphological parameters were observed for the largest CVEs, because they are the most heterogeneous and contain regions with low BV/TV as well.

3.2. Computation of the in situ stiffness tensor components

The strains of the embedded CVEs computed following the method described in section 2.4 are almost equivalent to the usual two-material approach. The average relative difference of all strain components between these two methods are only 0.08% (±0.91%) when KUBCs were directly applied on the CVE and 0.46% (±2.53%) when PMUBCs were applied. Accordingly, $\mathbf{S}^{\text{in situ}}$ was extrapolated from $\mathbf{S}_{\text{embed}}^{\text{KUBCs}}$ and $\mathbf{S}_{\text{embed}}^{\text{PMUBCs}}$ as presented in Fig. 4 for few representative components. The components of $\mathbf{S}_{\text{embed}}^{\text{KUBCs}}$ were larger than those of $\mathbf{S}_{\text{embed}}^{\text{PMUBCs}}$. Both stiffness tensors were affected by the thickness of the surrounding trabecular layer, but the rate of decrease of the $\mathbf{S}_{\text{embed}}^{\text{KUBCs}}$ components was lower than the rate at which the $\mathbf{S}_{\text{embed}}^{\text{PMUBCs}}$ components increased. The power law curves describing the dependency of the stiffness to the layer's thickness fitted well the KUBCs and PMUBCs data ($R^2 > 0.95$).

3.3. Size-dependency of the KUBCs, PMUBCs and in situ elastic properties

The exponents k (2.312) and l (1.313) were derived simultaneously for $\mathbf{S}^{\text{KUBCs}}$, $\mathbf{S}^{\text{PMUBCs}}$, $\mathbf{S}^{\text{in situ}}$ and all CVE sizes to evaluate their influence on the elasticity parameters (λ_0, λ_0', μ_0, E_0, ν_0). Despite this, the goodness of fit of the model to the µFE data was high for each size ($R_{adj}^2 \sim 0.9$), even if lower R_{adj}^2 were achieved with smallest CVEs (2.63 mm). The elasticity parameters under KUBCs, PMUBCs and *in situ* are provided for several CVE sizes in Table 2. Nevertheless, for both groups, all KUBCs and PMUBCs parameters (except ν_0) bounded the *in situ* values independently of the size. Except ν_0, KUBCs parameters decreased with growing size, while the PMUBCs ones (except λ_0) increased until 7.96 mm side length. Aside from the smallest CVEs, *in situ* values were almost constant. Fig. 5 better highlights the

relative effects of the boundary condition and size on the parameters E_0, μ_0 and ν_0. The convergence of μ_0 and E_0 was relatively slow for KUBCs and not reached for the largest CVEs. The relative differences are greater for μ_0 than E_0, especially for PMUBCs. Boundary condition and size had, however, moderate influence on ν_0.

4. Discussion

The homogenisation procedure conducted on a sample too small to be representative provides apparent properties affected by boundary condition and sample size. In an attempt to better approximate the effective properties of cancellous bone, we proposed to load an inner volume via the surrounding trabecular bone.

Prior studies attempted to measure the properties of cancellous bone "*in situ"* (Un et al. 2006, Harrison and McHugh 2010) and the concept of "embedded configuration" is not new. However, to our knowledge, this is the first time such technique is used to determine the homogenised properties of trabecular bone. µFE analyses of six different loading scenarios were performed to obtain the *in situ* stiffness tensor instead of focusing only on the elastic modulus along a single loading direction. Consequently, our results are much more general and include the shear moduli, independently of BV/TV and anisotropy. Secondly, we proposed a technique to reduce the computation time and convergence issues during the calculation of the strains applied to the embedded CVEs by avoiding the explicit modelling of the marrow phase. This assumption should not affect our findings as marrow has low stiffness in comparison to bone, especially under quasi-static loading. Third, we ensured the robustness of our findings by using trabecular biopsies originated from two common fracture sites (femur, vertebral body) and featuring a broad range of density and morphology. Finally, we verified the consistency of our results with respect to the spatial discretization of the solution by repeating a part of our analyses with a voxel mesh refined by a factor of two.

The size-dependency of the apparent elastic properties was evaluated via four CVE sizes. Our

results (Fig. 5, Table 2) confirm that *in situ* properties are essentially size-independent beyond a minimum of 2 to 4 mm and that KUBCs-based properties converge slower with the CVE size than when PMUBCs are used (Jiang et al. 2001, Blöß and Welsch 2015). The size-dependency of the KUBCs- and PMUBCs-based properties is a direct consequence of what happens at the boundary. Indeed, Fig. 4 shows that the effect of the boundary conditions is very localised and dissipates within 1 to 2 mm of bone. A similar effect (dubbed "side artefact" by the authors) was observed for cylindrical samples (Un et al. 2006, Bevill et al. 2007). Consequently, if the sample is smaller, the proportion of bone affected by the boundary conditions is larger and vice versa.

This work supports that PMUBCs are appropriate for mimicking the loading conditions of the trabecular core as suggested by Panyasantisuk et al. (2015). Other authors (Pahr and Zysset 2008, Blöß and Welsch 2015) inferred that PMUBCs were in fact the best boundary conditions for approximating the effective properties of cancellous bone regions. Nevertheless, PMUBCs-based properties slightly underestimate the *in situ* values even for our largest and nearly orthotropic CVEs. Furthermore, it is also worth noticing that the relative difference between the *in situ* and PMUBCs-based shear modulus is considerably larger than for elastic modulus. This finding is particularly important considering that bone yields more easily under shear. KUBCs, on the other hand, constrain the deformation of trabeculae near the faces of the RVE. This is somehow similar to the loading conditions near the cortical shell or a fully osseointegrated implant, except that a single face is usually constrained in those situations. "Real" elastic properties lay probably between *in situ* and KUBCs-based properties depending on both loading mode and stiffness of the surrounding tissue. This remains to be quantified in future works.

As we obtained the worst fit and largest errors for the smallest 2.63 mm CVEs, our analysis concur with previous recommendations. Those should be of approximately 5 mm edge length

to allow accurate calculation of the apparent elastic properties (van Rietbergen et al. 1995, Zysset et al. 1998). This size offers a good compromise between the computing resources needed for the µFE analyses and the relative homogeneity of the trabecular morphology (not achieved with smaller and much larger samples).

Several limitations should be highlighted. First, our complementary analyses (Appendix C) confirmed that the Hill condition is only approximately fulfilled for µFE analyses (Blöß and Welsch 2015). The lower difference between micro and macro-level energy after mesh refinement indicates that this is mainly a discretization issue of the FE method, even if a dependence on BV/TV was also observed (Fig. C1). Nevertheless, the reduction of element size did not alter the relative influence of BCs and CVE size on the apparent elastic properties as all parameters were affected similarly (Table C2). Other shortcomings are related to our large CVEs. Those were extracted from real cancellous bone and there is no guarantee for the trabecular morphology to be analogous within the inner core and in the outer trabecular region (Harrison and McHugh 2010). As it proved difficult to find large trabecular CVEs, only 20 biopsies were used, which is few compared to other studies (Gross et al. 2013, Panyasantisuk et al. 2015). Other relevant locations such as patella (Latypova et al. 2015) and distal radius (Gross et al. 2013) proved to be too small to extract sufficiently big volumes.

In this study, computational homogenisation of embedded trabecular regions was used to determine the *in situ* elastic properties of trabecular bone. Those were almost unaffected by the CVEs' dimensions and represent a close approximation of the effective properties. PMUBCs provide rather good, though lower, estimations of the *in situ* values, especially in shear. Similar analyses should be conducted beyond the linear range to provide more insights on the effective (BCs independent) yielding and failure behaviour of the trabecular structure.

References

Bevill G, Easley SK, Keaveny TM (2007) Side-artifact errors in yield strength and elastic modulus for human trabecular bone and their dependence on bone volume fraction and anatomic site. J Biomech 40(15): 3381-3388.

Böhm HJ (2016) A Short Introduction to Basic Aspects of Continuum Micromechanics, CDL–FMD Report 3–1998, TU Wien, Vienna. (https://www.ilsb.tuwien.ac.at/links/downloads/ilsbrep206.pdf)

Blöß T, Welsch M (2015) RVE Procedure for Estimating the Elastic Properties of Inhomogeneous Microstructures Such as Bone Tissue. Biomedical Technology 74:1-17. Springer.

Choi K, Kuhn JL, Ciarelli MJ, Goldstein SA (1990) The elastic moduli of human subchondral, trabecular, and cortical bone tissue and the size-dependency of cortical bone modulus. J Biomech 23(11):1103-1113.

Eringen AC (1999) Microcontinuum Field Theories I: Foundations and Solids. Springer-Verlag, New York.

Flaig C (2012) A highly scalable memory efficient multigrid solver for µ-finite element analyses. Doctoral dissertation, Eidgenössische Technische Hochschule (ETH) Zürich.

Gross T, Pahr DH, Zysset PK (2013) Morphology–Elasticity Relationships Using Decreasing Fabric Information of Human Trabecular Bone From Three Major Anatomical Locations. Biomech Model Mechanobiol 12(4):793–800.

Hadji P, Klein S, Gothe H, Häussler B, Kless Th, Schmidt T, Steinle Th, Verheyen F, Linder R (2013) The epidemiology of osteoporosis—Bone Evaluation Study (BEST): an analysis of routine health insurance data. Dtsch Arztebl Int 110(4):52–7.

Harrigan TP, Mann RW (1984) Characterization of Microstructural Anisotropy in Orthotropic Materials Using a Second Rank Tensor. J Mater Sci 19(3):761–767.

Harrison NM, McHugh PE (2010) Comparison of trabecular bone behavior in core and whole bone samples using high-resolution modeling of a vertebral body. Biomech Model Mechanobiol 9(4):469-480.

Hazanov S, Amieur M (1995) On overall properties of elastic heterogeneous bodies smaller than the representative volume. Int J Eng Sci 33(9):1289–1301.

Hazanov S, Huet C (1994) Order relationships for boundary conditions effect in heterogeneous bodies smaller than the representative volume. J Mech Phys Solids 42(12):1995–2011.

Hill R (1963) Elastic properties of reinforced solids: some theoretical principles. J Mech Phys Solids 11:127–140.

Hollister SJ, Fyhrie DP, Jepsen KJ, Goldstein SA (1991) Application of homogenization theory to the study of trabecular bone mechanics. J Biomech 24(9):825-839.

Hollister SJ, Kikuchi N (1992) A comparison of homogenization and standard mechanics analyses for periodic porous composites. Comput Mech 10:73-95.

Hütter G (2016) Application of a microstrain continuum to size effects in bending and torsion of foams. Int J Eng Sci 101:81-91.

Jiang M, Alzebdeh K, Jasiuk I, Ostoja-Starzewski M (2001) Scale and Boundary Conditions Effects in Elastic Properties of Random Composites. Acta Mech 148:63–78.

Keaveny TM, McClung MR, Genant HK, Zanchetta JR, Kendler D, Brown JP, Goemaere S, Recknor C, Brandi ML, Eastell R, Kopperdahl DL, Engelke K, Fuerst T, Radcliffe HS, Libanati C (2014) Femoral and vertebral strength improvements in postmenopausal women with osteoporosis treated with denosumab. J Bone Miner Res 29(1):158-165.

Lakes RS (1983) Size effects and micromechanics of a porous solid. J Mater Sci 18:2572–2580.

Latypova A, Maquer G, Elankumaran K, Pahr D, Zysset P, Pioletti DP, Terrier A (2016). Identification of elastic

properties of human patellae using micro-finite element analysis. J Biomech doi:10.1016/j.jbiomech.2016.07.031

Lochmüller EM, Pöschl K, Würstlin L, Matsuura M, Müller R, Link TM, Eckstein F (2008) Does thoracic or lumbar spine bone architecture predict vertebral failure strength more accurately than density? Osteoporosis Int 19(4):537-545.

Maquer G, Musy SN, Wandel J, Gross T, Zysset PK (2015) Bone volume fraction and fabric anisotropy are better determinants of trabecular bone stiffness than other morphological variables. J Bone Miner Res 30(6):1000-1008.

Maquer G, Bürki A, Nuss K, Zysset PK, Tannast M (2016) Head-Neck Osteoplasty has Minor Effect on the Strength of an Ovine Cam-FAI Model: In Vitro and Finite Element Analyses. Clin Orthop Relat Res. doi:10.1007/s11999-016-5024-8.

Marangalou JH, Ito K, Cataldi M, Taddei F, & van Rietbergen, B. (2013). A novel approach to estimate trabecular bone anisotropy using a database approach. J Biomech 46(14), 2356-2362.

Ostoja-Starzewski M (1998) Random field models of heterogeneous materials. Int J Solids Structures 35(19):2429–2455.

Ostoja-Starzewski M (2006) Material spatial randomness: from statistical to representative volume element. Probab Eng Mech 21(2):112–132.

Pahr DH, Zysset P (2008) Influence of boundary conditions on computed apparent elastic properties of cancellous bone. Biomech Model Mechanobiol 7(6):463–476.

Panyasantisuk J, Pahr DH, Gross T, Zysset PK (2015) Comparison of mixed and kinematic uniform boundary conditions in homogenized elasticity of femoral trabecular bone using microfinite element analyses. J Biomech Eng 137(1):011002.

Pecullan S, Gibiansky LV, Torquato S (1999) Scale Effects on the Elastic Behavior of Periodic and Hierarchical Two-Dimensional Composites. J Mech Phys Solids 47:1509–1542.

Pistoia W, Van Rietbergen B, Lochmüller E-M, Lill C, Eckstein F, Rüegsegger P (2002) Estimation of Distal Radius Failure Load With Micro-Finite Element Analysis Models Based on Three-Dimensional Peripheral Quantitative Computed Tomography Images. Bone 30(6):842–848.

Riedler TW, Calvard S (1978) Picture Thresholding Using an Iterative Selection Method. IEEE Trans Systems, Man Cybern 8(8):630–632.

Synek A, Chevalier Y, Baumbach SF, Pahr DH (2015) The influence of bone density and anisotropy in finite element models of distal radius fracture osteosynthesis: Evaluations and comparison to experiments. J Biomech 48(15):4116-4123.

Syroka-Korol E, Tejchman J, Mróz Z (2013) FE calculations of a deterministic and statistical size effect in concrete under bending within stochastic elasto-plasticity and non-local softening. Eng Struct 48:205-219.

Un K, Bevill G, Keaveny TM (2006) The Effects of Side-Artifacts on the Elastic Modulus of Trabecular Bone. J Biomech 39(11):1955–1963.

van Rietbergen B, Weinans H, Huiskes R, Odgaard A (1995) A new method to determine trabecular bone elastic properties and loading using micromechanical finite-element models. J Biomech 28(1):69-81.

Viceconti M (2015) Biomechanics-based in silico medicine: The manifesto of a new science. J Biomech 48(2):193-194.

Wang C, Feng L, Jasiuk I (2009) Scale and Boundary Conditions Effects on the Apparent Elastic Moduli of Trabecular Bone Modeled as a Periodic Cellular Solid. J Biomech Eng 131(12):121008.

Wheel MA, Frame JC, Riches PE (2015) Is smaller always stiffer? On size effects in supposedly generalized continua. International Journal of Solids and Structures 67-68:84-92.

Whitehouse WJ (1974) The Quantitative Morphology of Anisotropic Trabecular Bone. J Microsc 101(2):153–

168.

Zysset P, Curnier A (1995) An Alternative Model for Anisotropic Elasticity Based on Fabric Tensors. Mech Mater 21(4):243–250.

Zysset P, Goulet, RW, Hollister SJ (1998) A global relationship between trabecular bone morphology and homogenized elastic properties. J Biomech Eng 120(5): 640-646.

Zysset PK (2003) A Review of Morphology–Elasticity Relationships in Human Trabecular Bone: Theories and Experiments. J Biomech 36(10):1469–1485.

Zysset PK, Dall'Ara E, Varga P, Pahr DH (2013) Finite element analysis for prediction of bone strength. BoneKEy reports, 2.

Figure captions

Fig. 1. a) A large trabecular volume is cropped from the µCT scan of a vertebral body or a femoral head. It is turned into a µFE model on which loads are applied. The apparent stiffness of the inner core is then measured, the outer layer acting as a buffer transmitting the loads. b) The boundary conditions (here KUBCs and PMUBCs) applied on the outer region still influence the stiffness of the core region. Our assumption is that the KUBCs- and PMUBCs-based stiffness of the core would converge towards the constant "*in situ"* value if the outer region were sufficiently large.

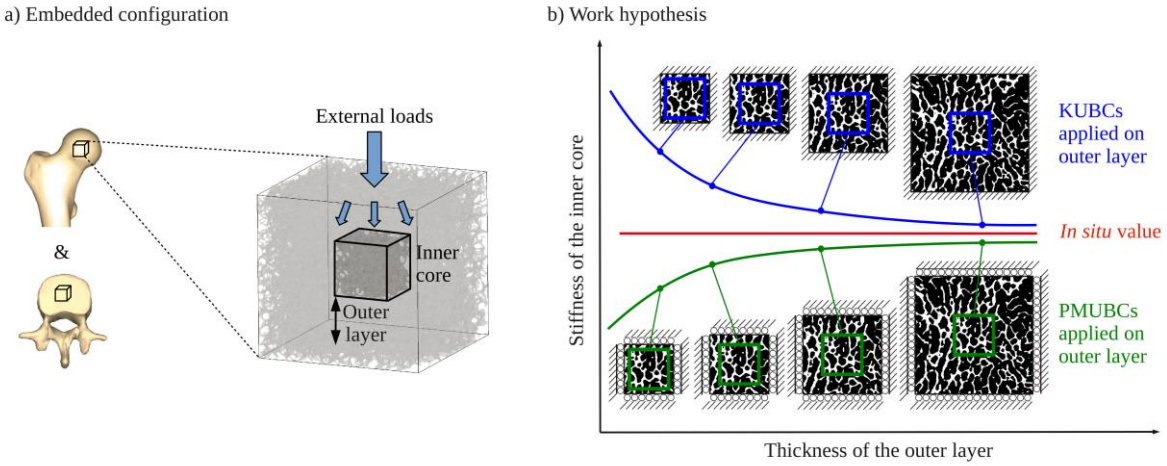

Fig. 2. One goal of the study is to verify our hypothesis for different CVE sizes. *In situ*, KUBCs- and PMUBCs-based apparent elastic properties were thus determined for four CVE sizes. *In situ* properties were in fact derived for CVEs embedded in larger and larger CVEs loaded under KUBCs and PMUBCs. The thickness of the outer layer of trabecular bone is thus progressively increased as described in Fig. 1. The maximal thickness reached for each CVE is also provided.

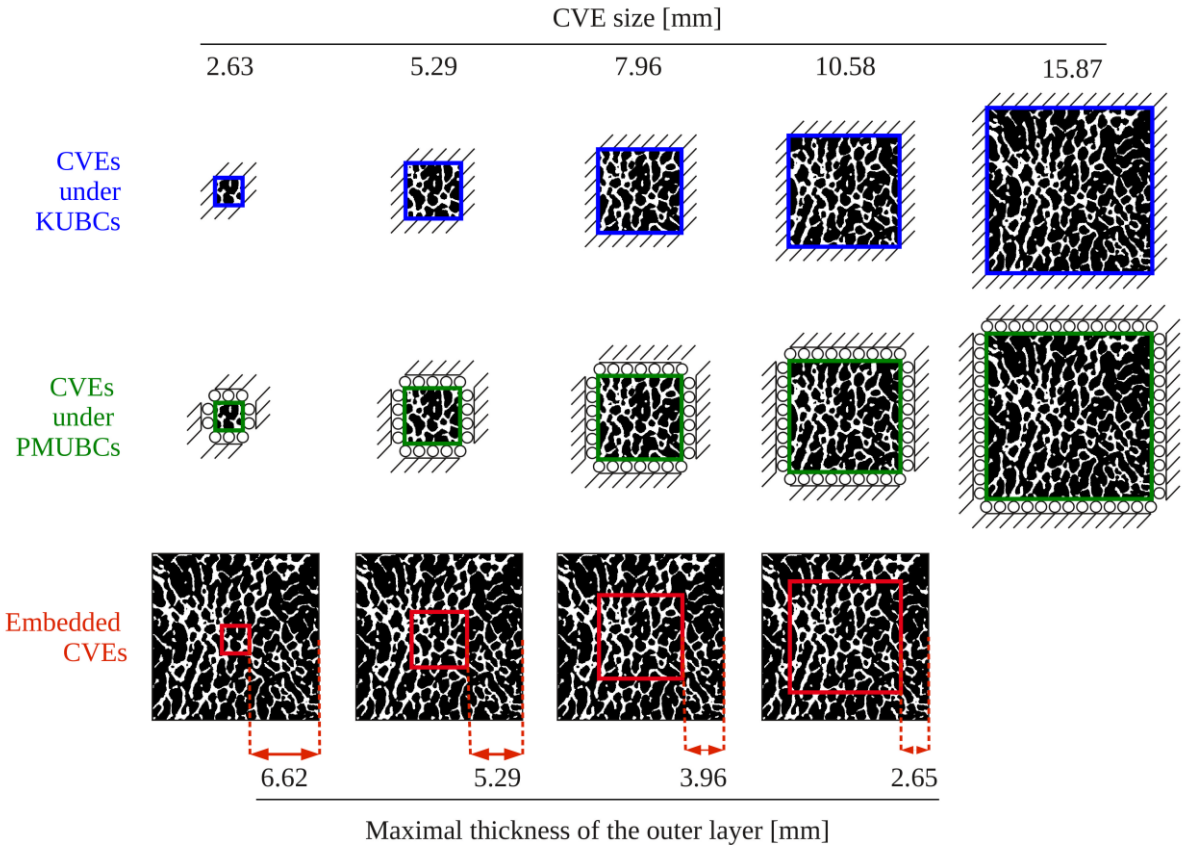

Fig. 3. Computation of the strains in the virtual marrow. a) Faces of the CVE as described in Pahr and Zysset (2008), b) The displacement $\overline{u}$ of the virtual marrow point are interpolated from the closest neighbouring bone nodes in east, west, north, south, top and bottom directions.

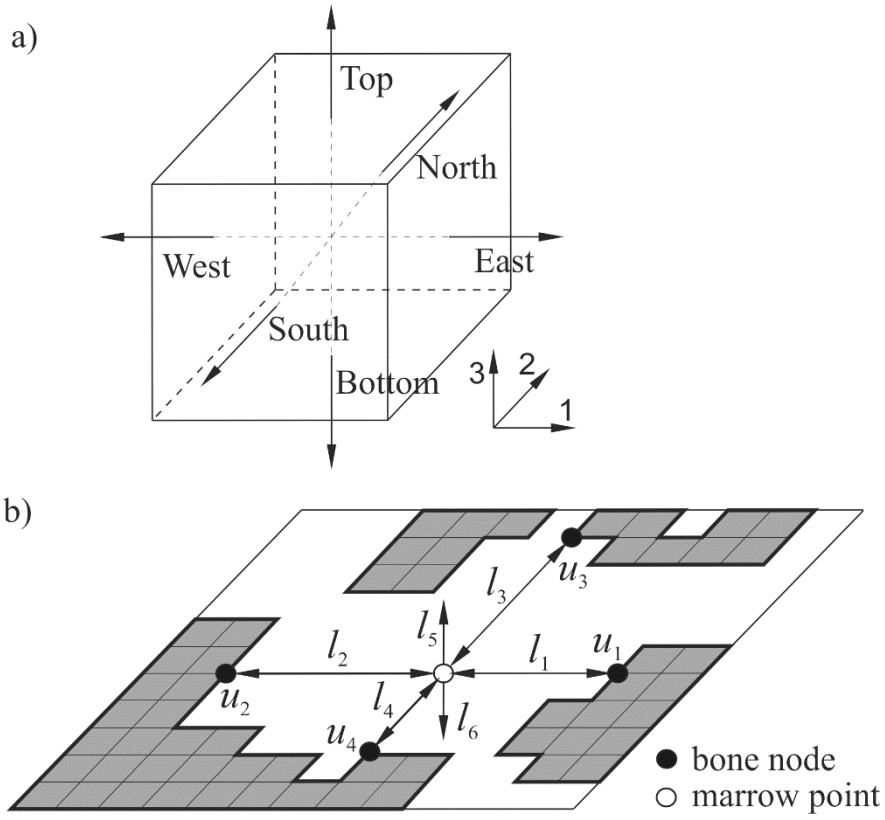

Fig. 4. Computation of the *in situ* stiffness tensor components. The *in situ* components of the stiffness tensor ($\mathbf{S}^{\text{in situ}}$) were computed as the asymptotic value towards which the components of the KUBCs ($\mathbf{S}_{\text{embed}}^{\text{KUBCs}}$) and PMUBCs ($\mathbf{S}_{\text{embed}}^{\text{PMUBCs}}$)-based stiffness tensors converge. This example is displaying the convergence of the main normal component λ_{11} (a, b), the off-diagonal normal component λ_{12} (c, d) and the shear component μ_{12} (e, f) for 5.29 mm CVEs extracted from a vertebra and a femur.

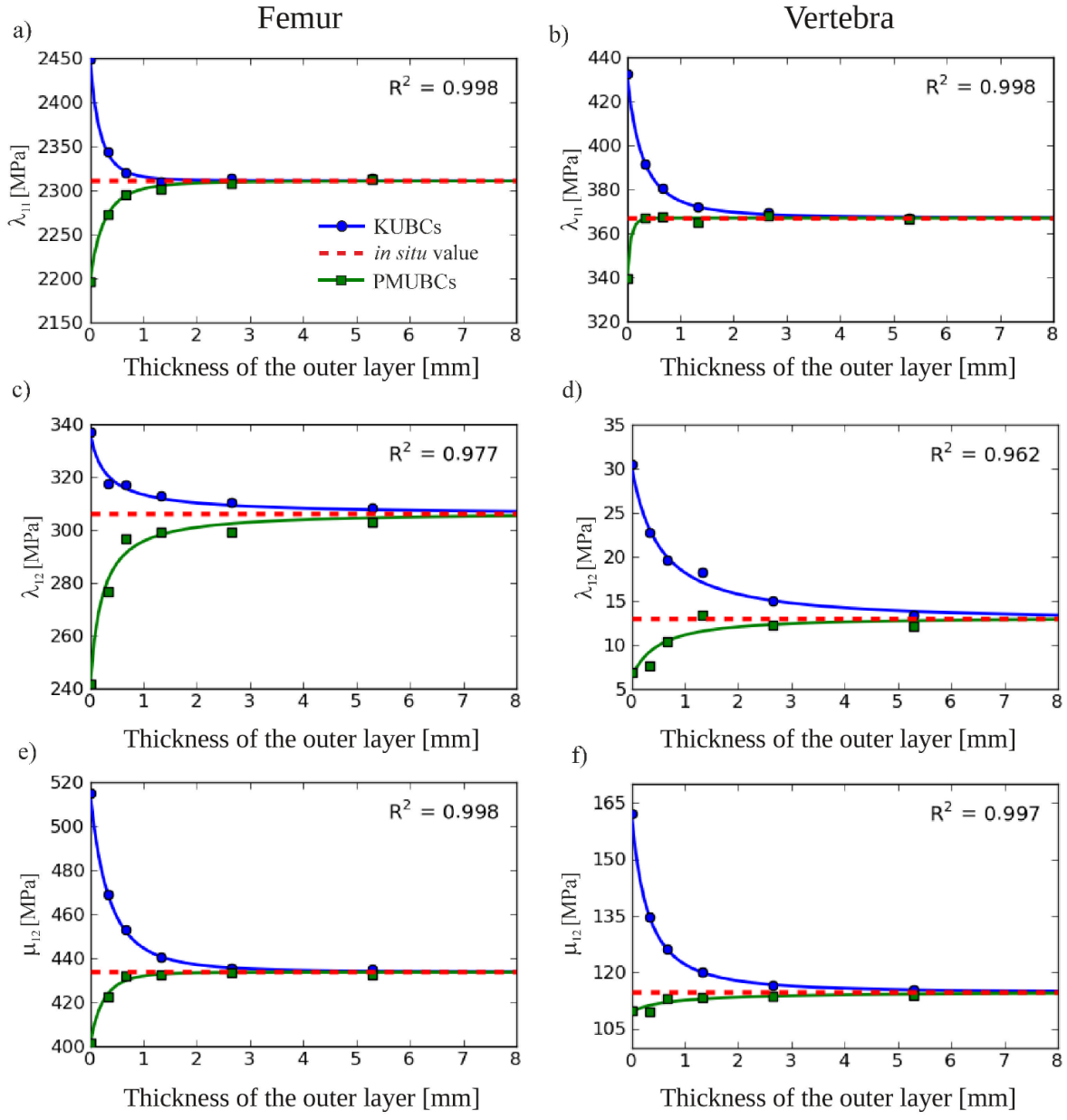

Fig. 5. Size-dependency of the KUBCs, PMUBCs and *in situ* elastic properties. Elastic modulus (E_0), shear modulus (μ_0) and Poisson ratio (ν_0) computed for different CVE sizes on the complete data set are displayed relative to the *in situ* values of the 5.29 mm CVEs (E_{ref}, μ_{ref}, ν_{ref}). KUBCs- and PMUBCs-based E_0 and μ_0 bound the *in situ* values. BCs and CVE size have moderate impact on ν_0. The confidence intervals of the measures were also computed.

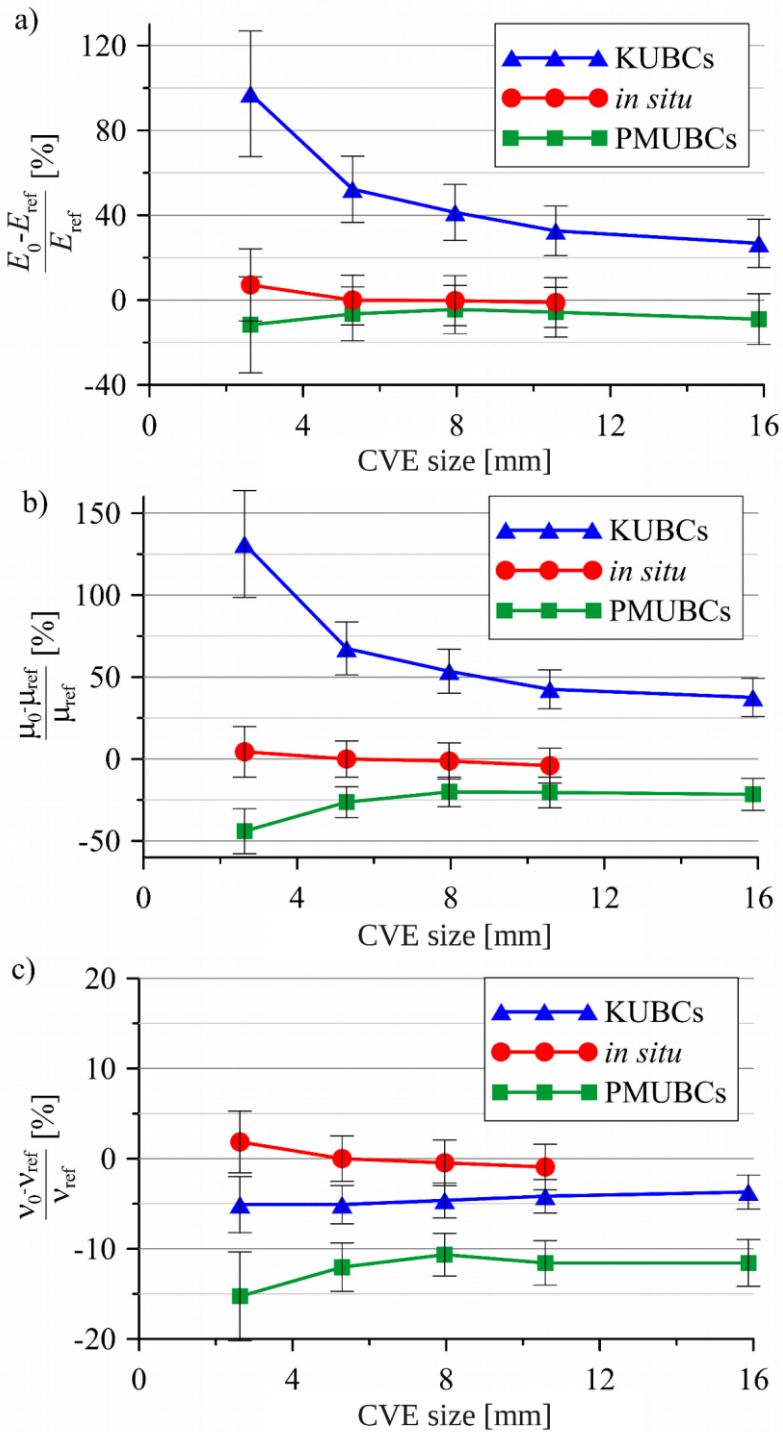

Tables

Table 1. Bone volume fraction (BV/TV) and degree of anisotropy (DA) for the different CVE sizes for the complete and femur data sets. Average BV/TV and DA and their standard deviations decrease with increasing size.

CVE size [mm]	complete data set		femur data set	
	BV/TV	DA	BV/TV	DA
2.63	0.204 (±0.101)	1.63 (±0.20)	0.253 (±0.077)	1.59 (±0.15)
5.29	0.202 (±0.097)	1.60 (±0.19)	0.256 (±0.069)	1.61 (±0.19)
7.96	0.198 (±0.088)	1.59 (±0.18)	0.248 (±0.057)	1.62 (±0.19)
10.58	0.192 (±0.082)	1.58 (±0.17)	0.240 (±0.048)	1.62 (±0.18)
15.87	0.175 (±0.068)	1.53 (±0.14)	0.215 (±0.030)	1.56 (±0.13)

Table 2. Comparison of *in situ*, KUBCs- and PMUBCs-based elasticity parameters for different CVE sizes. In this table, *k* (2.3116) and *l* (1.313) were fixed to allow the comparison.

CVE size [mm]	λ_0	λ_0'	μ_0	E_0	v_0	R^2_{adj}
KUBCs, complete data set						
2.63	15390	10400	12460	36044	0.205	0.834
5.29	13069	8028	9023	27821	0.205	0.936
7.96	12371	7504	8272	25824	0.206	0.946
10.58	11790	7066	7680	24232	0.207	0.956
15.87	11158	6808	7414	23158	0.208	0.955
KUBCs, femur data set						
2.63	11378	8605	9946	27557	0.216	0.884
5.29	10015	7337	8112	23033	0.219	0.912
7.96	9753	7196	7783	22135	0.221	0.914
10.58	9516	7121	7639	21616	0.223	0.917
15.87	9301	7190	7760	21590	0.225	0.928
In situ, complete data set						
2.63	11081	6283	5625	19573	0.220	0.902
5.29	9957	5710	5389	18269	0.216	0.942
7.96	10011	5655	5321	18221	0.215	0.940
10.58	10091	5553	5170	18057	0.214	0.940
In situ, femur data set						
2.63	8776	6594	6068	17750	0.240	0.905
5.29	8380	6254	6000	17443	0.235	0.923
7.96	8410	6169	6042	17640	0.231	0.922
10.58	8593	6113	5926	17632	0.230	0.932
PMUBCs, complete data set						
2.63	11548	3944	3016	16135	0.183	0.841
5.29	10827	4414	3969	17084	0.190	0.933
7.96	10618	4591	4306	17462	0.193	0.943
10.58	10355	4468	4289	17228	0.191	0.940
15.87	9819	4314	4226	16623	0.191	0.928
PMUBCs, femur data set						
2.63	10147	4537	4046	16430	0.199	0.929
5.29	8898	4993	4794	16361	0.213	0.948
7.96	8993	5176	5042	16868	0.213	0.955
10.58	8982	5085	5072	16989	0.210	0.950
15.87	8792	4891	5032	16840	0.206	0.930

Appendix A

Table A1. For further use of the Zysset-Curnier model, *in situ*, PMUBCs- and KUBCs-based elastic parameters were calculated independently for each CVE size on the complete data set. The high values of *k* and *l* were obtained for PMUBCs, confirming the large impact of BV/TV and anisotropy on elastic parameters for these BCs.

CVE size [mm]	λ_0	λ_0'	μ_0	k	l	R^2_{adj}
			KUBCs			
2.63	4470	3021	3619	1.616	0.904	0.977
5.29	6351	3901	4384	1.903	1.093	0.972
7.96	6875	4170	4597	1.981	1.102	0.969
10.58	8413	5042	5480	2.126	1.124	0.963
15.87	10279	6272	6830	2.269	1.220	0.955
			In situ			
2.63	9381	5318	4762	2.215	1.402	0.904
5.29	11318	6490	6126	2.385	1.336	0.943
7.96	11626	6567	6179	2.397	1.302	0.941
10.58	13238	7285	6783	2.465	1.289	0.943
			PMUBCs			
2.63	29494	10074	7704	2.835	1.820	0.870
5.29	15692	6398	5753	2.519	1.543	0.940
7.96	15277	6606	6196	2.518	1.381	0.949
10.58	17623	7603	7300	2.609	1.369	0.950
15.87	18229	8009	7847	2.642	1.499	0.941

Appendix B

Table B1. The Zysset-Curnier model parameters computed under KUBCs and PMUBCs for 5.29 mm CVEs are compared with other works (Gross et al. 2013, Panyasantisuk et al. 2015). The values of k and l were taken from the corresponding literature to allow for direct comparisons. The good correspondence of our parameters with the literature data confirms the correctness of the applied methodology. The parameters λ_0, λ_0', μ_0 computed in this study are lower than values reported in literature.

Reference	Location	λ_0	λ_0'	μ_0	k	l	R^2_{adj}
				KUBCs			
Present study	**femur, vertebra**	**3878**	**2382**	**2677**	**1.62**	**1.10**	**0.955**
Gross et al. 2013	femur, vertebra, radius	4152	2932	2892	1.62	1.10	0.960
Present study	**femur**	**3649**	**2673**	**2956**	**1.60**	**0.99**	**0.967**
Gross et al. 2013	femur	3841	3076	3115	1.60	0.99	0.983
Panyasantisuk et al. 2015	femur	3306	2736	2837	1.55	0.82	0.985
				PMUBCs			
Present study	**femur**	**5027**	**2821**	**2708**	**1.91**	**1.10**	**0.935**
Panyasantisuk et al. 2015	femur	5060	3353	3117	1.91	1.10	0.970

Appendix C

An extra analysis was performed on the complete data set after mesh refinement of the 2.63, 5.29, 7.96 and 10.58 mm CVEs. Each hexahedral finite element from the original mesh (37 μm size) was divided into eight smaller elements (18.5 μm size). The Zysset-Curnier model was then fitted to the KUBCs, PMUBCs and *in situ* stiffness tensors to evaluate the impact of the refinement (Table C1, Table C2). To verify the impact of the mesh on the Hill condition, the average of the product of the stress and strain tensors for all elements (internal strain energy U_{micro}) and the product of the stress and strain averages (macro-level strain energy U_{macro}) were computed. The relative difference between U_{micro} and U_{macro} for 5.29 mm IVEs as a function of BV/TV is presented in Fig. C1.

Table C1. The Zysset-Curnier model parameters calculated for 5.29 mm CVEs after mesh refinement. A small increase of *k* and *l* is noticeable.

	λ_0	λ_0'	μ_0	k	l	R^2_{adj}
KUBCs	6462	3887	4407	1.943	1.120	0.972
In situ	11513	6431	6139	2.426	1.405	0.946
PMUBCs	16148	6448	5767	2.568	1.577	0.940

Table C2. The relative changes of the Zysset-Curnier model parameters after mesh refinement computed for constant k=2.3116 and l=1.313. The relative difference is very consistent across CVE sizes and stiffness tensors.

CVE size [mm]	λ_0	λ_0'	μ_0	E_0	v_0
		KUBCs			
2.63	-8.4%	-10.1%	-8.7%	-8.2%	-1.4%
5.29	-7.7%	-9.6%	-8.8%	-8.1%	-1.1%
7.96	-7.6%	-9.5%	-8.8%	-8.1%	-1.0%
10.58	-7.6%	-9.5%	-8.9%	-8.1%	-1.0%
		In situ			
2.63	-5.8%	-6.8%	-7.6%	-6.7%	0.0%
5.29	-5.7%	-7.3%	-7.5%	-6.5%	-0.6%
		PMUBCs			
2.63	-8.1%	-8.0%	-10.6%	-9.1%	0.8%
5.29	-8.1%	-10.0%	-10.5%	-8.9%	-0.8%
7.96	-8.0%	-10.0%	-10.3%	-8.8%	-0.8%
10.58	-8.0%	-10.0%	-10.3%	-8.8%	-0.9%

Fig. C1. The relative difference between internal strain energy U_{micro} and macro-level strain energy U_{macro} before and after mesh refinement as a function of BV/TV for a) KUBCs, b) *in situ*, c) PMUBCs. The Hill condition is only approximately fulfilled. The difference between strain energy at macro- and micro-level decreases after mesh refinement and with increasing BV/TV.